A low-dissipative and accurate method of simulating the unsteady mixing process

Gao, Yunhu; Wang, Zhong-Nan; Xu, Zhihong

DOI:
10.1016/j.cej.2023.141760

Document Version
Publisher's PDF, also known as Version of record

Citation for published version (Harvard):
Gao, Y, Wang, Z-N & Xu, Z 2023, 'A low-dissipative and accurate method of simulating the unsteady mixing process', *Chemical Engineering Journal*, vol. 460, 141760. https://doi.org/10.1016/j.cej.2023.141760

Chemical Engineering Journal 460 (2023) 141760

Contents lists available at ScienceDirect

Chemical Engineering Journal

journal homepage: www.elsevier.com/locate/cej

Short communication

A low-dissipative and accurate method of simulating the unsteady mixing process

Yunhu Gao [a,*], Zhongnan Wang [b], Zhihong Xu [c,*]

[a] Department of Engineering, University of Cambridge, Trumpington Street, CB2 1PZ Cambridge, UK
[b] College of Engineering and Physical Sciences, University of Birmingham, Edgbaston, B15 2TT Birmingham, UK
[c] Suzhou Sicui Institute of Isotope Technology Company, Ltd., Fuyu Road, 215522 Suzhou, China

ARTICLE INFO

Keywords:
Unsteady mixing
Numerical diffusion
Backward particle tracking
T mixer
Mixing index

ABSTRACT

Micro/milli-reactors have been widely used because of their advantages, *e.g.*, intrinsic safety, fast heat transfer and exquisite control of the reaction conditions. However, the mixing efficiency in microreactors is often limited by slow molecular diffusion in steady laminar flow. The mixing efficiency is higher in the unsteady state, but the lack of an accurate simulation method for unsteady mixing limits the development of highly efficient mixers. Thus, this work establishes a new method to precisely simulate the unsteady mixing process, without being affected by numerical diffusion, based on the Lagrangian scalar transport equation. The method is validated by experimental results. Sensitivity analyses are conducted to confirm the simulation results. The accurate simulation of the mixing process will reduce the number of experiments, hence accelerating the development of highly efficient mixers.

1. Introduction

Continuous flow micro/milli-reactors are widely used in various applications, *e.g.*, smart material synthesis, sensors and organic synthesis, owing to the following advantages provided by their small sizes: fast heat transfer, less waste, and intrinsic safety [1–3]. Despite the small diameter of the reactors, the performance of the reactors is often subject to the mixing efficiency, since the mass transfer in the radial direction is controlled by slow molecular diffusion rather than convection in steady laminar flow. For example, the selectivity of rapid intramolecular rearrangements can be tuned by efficient mixing [4]; the size of active pharmaceutical ingredients nanoparticles can be reduced at a high mixing efficiency to achieve higher solubility [5]; the size of nanoparticles is adjusted by manipulating the mixing efficiency in microreactors [6–8].

Mixing efficiency has been studied by both experimental and numerical approaches. The concentration profiles on cross-sectional planes of the channel can be captured by planar laser-induced fluorescence [9–11]. But the technology is expensive and time-consuming. The Villermaux-Dushmann (VD) reaction is a well-known model reaction whose selectivity is sensitive to mixing efficiency [12,13]. The VD reaction is used to compare the efficiency of different mixers, however, insight into the fluid field is not available. Numerical methods are widely adopted to gain more understanding of the mixing processes at a low cost. However, the simulated mixing efficiency by commercial software is highly overestimated because of numerical diffusion, arising from the truncation errors in representing the flow field in a discretised form [4,14]. A method based on the Lagrangian species transport equation was developed by Matsunaga *et al.* to accurately simulate the mixing efficiency in micromixers [15]. However, this method is limited to the steady state. In other words, Re number is limited to a small range. Taking a *T*-mixer with a rectangular cross-section for example, Dreher *et al.* pointed out that the flow field in the T mixer is steady when Re is smaller than 237, exhibiting strictly laminar flow, Dean vortex and engulfment flow at different Re numbers. As Reynolds number further increases, the flow field develops from the steady state to a transient state with periodic fluctuation and quasi-periodic fluctuation before turbulence [16–18]. The mixing efficiency can also be accurately simulated by the random walking particle tracking method based on the Lagrangian scalar transport equation [19–21], which is more computationally expensive than Matsunaga's method [15,20] and is not used for the simulation of unsteady mixing process in microreactors yet. This mixing efficiency in the T mixer has been experimentally recorded by Zhang *et al.* [22], whose results are used to validate our simulation in this study. It is worth noting that a higher mixing efficiency is achieved

* Corresponding authors.
E-mail addresses: yg327@cam.ac.uk (Y. Gao), xuzhihong@sc-iso.org (Z. Xu).

https://doi.org/10.1016/j.cej.2023.141760
Received 1 November 2022; Received in revised form 2 January 2023; Accepted 4 February 2023
Available online 8 February 2023

Nomenclature

A	Area of the cross section, m^2
C_A	Concentration of the tracer Rhodamine 6G, mol/m^3
$\overline{C_A}$	Average concentration of the tracer, mol/m^3
$\not{D}$	Diffusion coefficient of Rhodamine 6G, m^2/s
d	Channel width, m
f	Normalized concentration of the tracer
MI	Mixing index
MP	Mixing potential, m^2/m^3
N_i	The number of sampling particles in the z direction
N_j	The number of sampling particles in the x direction
$n_{T,ff}$	The last saved flow fields for $n_{\tau,con}$
$N_{T,ff}$	The number of all saved flow fields
$n_{\tau,con}$	The number of concentration profile being calculated
$N_{\tau,con}$	Total number of frames in the video
p	Pressure, Pa
Re	Reynolds number
t	Time, s
$\overline{T}_{i,j}$	The travelling time of particle (i,j)
$\overline{u}$	The average velocity at the inlet, m/s
$\vec{u}$	Velocity vector, m/s
$\vec{u_w}$	Water velocity vector, m/s
u_p	The velocity component perpendicular to the cross section, m/s
$\dot{V}$	Volumetric flowrate, m^3/s
x	X direction
y	Y direction
z	Z direction
δ	Layer thickness of the laser source, mm
μ	Viscosity, Pa·s
ρ	Density, kg/m^3
σ^2	Concentration variance on the cross section, mol^2/m^6
ΔT	The time interval between two saved flow fields
$\Delta\tau$	The time interval between two concentration profiles in the video

Subscript

con	Concentration
i	The sequence of sampling particle in the z direction
j	The sequence of sampling particle in the x direction
$npar$	The total number of sampling particles
τ	The time to capture concentration profiles on the interested cross section
T	The time of flow field

in an unsteady mixing process at a higher Re number as convection is intensified, compared with the mixing process at the steady state. Thus, the accurate simulation of the dynamic mixing process is vital to develop more efficient mixers.

In this paper, a new method is proposed to accurately simulate the concentration distributions in a T mixer under the unsteady state, in the absence of numerical diffusion for the concentration field. The method discretizes the unsteady flow field to simulate convection based on the Lagrangian scalar transport equation and adopts Matsunaga's method to estimate diffusion. The method is validated by experimental results. Then sensitivity analyses are conducted to confirm the simulation results.

2. Simulation methods

The mixing process inside a T mixer (Fig. 1) is simulated. The T mixer has two inlets with equal flowrates for fresh water and 0.15 mg/L Rhodamine 6G, respectively. This method simulates the concentration distribution of the tracer, Rhodamine 6G, in the unsteady mixing process in the T mixer (Fig. 1) without taking chemical reactions into account. The *T*-mixer is of the same size as the experiment by Zhang *et al.* [22]. The origin of the coordinate system is in the middle of the channel (Fig. 1a). Reynolds number, $Re = \rho d\overline{u}/\mu$, at the inlet is 237 in both the experiment and the simulation. Since the tracer concentration is very low, the physical properties of the fluid are set as these of water at 15 °C.

Three steps are needed to accurately simulate the unsteady dynamic

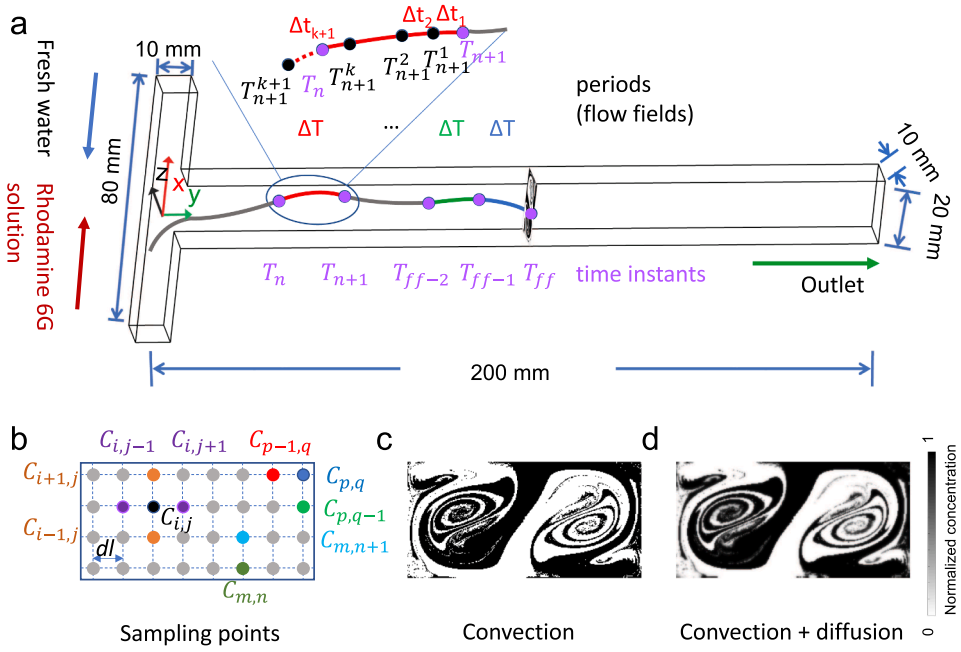

Fig. 1. A) The size of the T mixer and illustration of backward particle tracking through a series of time steps and flow fields. b) An exemplary array of sampling points (8 × 4) set on the interested cross-sectional plane. c) The simulated concentration distribution by convection (sampling points 300 × 150) at Re 237 and y = 25 mm. d) The calculated concentration distribution with the contributions of convection and diffusion. Conditions: water temperature 15 °C, the diffusion coefficient of Rhodamine 6G 2.1 × 10^{-10} m^2/s, inlet Re 237, sampling points 300 × 150, 3 million grids.

mixing process: i. simulate the unsteady velocity field; ii. obtain the convection contributed concentration profile simulated using backward particle tracking; iii. estimate the contribution of molecular diffusion. A flow diagram is present in Fig. 2 to illustrate the method.

Firstly, the unsteady flow field is simulated by solving the incompressible Navier-Stokes equations (Eqs. (1) and (2)). The hexahedral mesh with 3 million grids is drawn by ICEM. The fully developed velocity distribution at the inlet is provided by user-defined functions [23]. Non-slip boundary conditions are adopted. The outlet pressure is set as 0 gauge pressure. The SIMPLE algorithm is used to iterate the velocity and pressure field [24] and the least squares cell based spatial discretization scheme to calculate the gradient. The second order scheme and third order QUICK scheme are adopted to discretise pressure and momentum, respectively. The second order implicit scheme is used for time discretization. Given that the simulated period of fluctuation is 1.72 s at Re 237, the time step is set as 0.01 s, and the velocity field is saved every-five steps, implying a time interval ΔT of 0.05 s between two saved velocity fields.

$$\nabla \bullet \overrightarrow{u} = 0 \tag{1}$$

$$\rho \frac{D\overrightarrow{u}}{Dt} = -\nabla p + \mu \nabla^2 \overrightarrow{u} \tag{2}$$

where, ρ is the density of water, 999.19 kg/m^3 at 15 °C, μ denotes viscosity of water, p is pressure, t represents time.

To avoid the numerical diffusion arising from the truncation errors in representing the flow field in a discretised form, the Lagrangian scalar transport equation (Eq. (3)) is solved by the discrete phase model rather than the Eulerian scalar transport equation. This is essential to control the effect of numerical dissipation.

$$\frac{DC_A}{Dt} = D\nabla^2 C_A \tag{3}$$

where, C_A is the concentration of Rhodamine 6G, D denotes the diffusion coefficient of Rhodamine 6G.

Secondly, a time series of convection-contributed concentration profiles (total number of frames: $N_{\tau,con}$) are obtained from the unsteady flow simulation. The time interval $\Delta\tau$ between two captured concentration profiles is 0.1 s in the experimental measurement [22]. The concentration is calculated with the same time interval of $\Delta\tau$ at an interested cross-sectional plane. For each concentration profile, an array of sampling particles (total number of sampling particles: $N_j \times N_i = 300 \times 150$, Fig. 1b) is set at the interested cross-sectional plane at moment T_{ff}. The initial concentrations of the sampling particles are obtained by tracking them backward to their sources, through a series of velocity fields saved in step 1 (flow simulation), with a fixed time interval ΔT between two velocity fields of 0.05 s. During each time interval, the drag force on a sampling particle, $\overrightarrow{F_d}$, is calculated by reversing the direction of the velocity of water, $\overrightarrow{u_w}$, adopting the discrete phase model and user-defined functions, as shown in Eq. (4). The diameter of the sampling particles, d_p, is set as 1 % of the channel width (0.1 mm), and the density of the particle, ρ_p, is set as that of water at 15 °C, 999.19 kg/m^3 [15]. The acceleration rate of the particle, $\overrightarrow{a}$, is calculated by the dividing the drag force by the particle mass in Eq. (5). Thus, the velocity of the particle can be calculated by integrating the acceleration rate of the particle. Furthermore, the position of the particle is calculated by integrating the velocity with the discrete phase model. For each velocity field, each sampling particle is tracked 100 steps, with the Runge-Kutta scheme (accuracy 10^{-5}), to ensure that most of the sampling particle have a longer traveling time than 0.05 s. After the particle tracking in period n, the pathlines of the sampling particles are exported by Fluent and analysed by an in-house Matlab code. In the time period between T_n and T_{n+1}, the velocity and position of the sampling point at T_n are linearly interpolated by the velocities and positions at T^k_{n+1} and T^{k+1}_{n+1} shown in

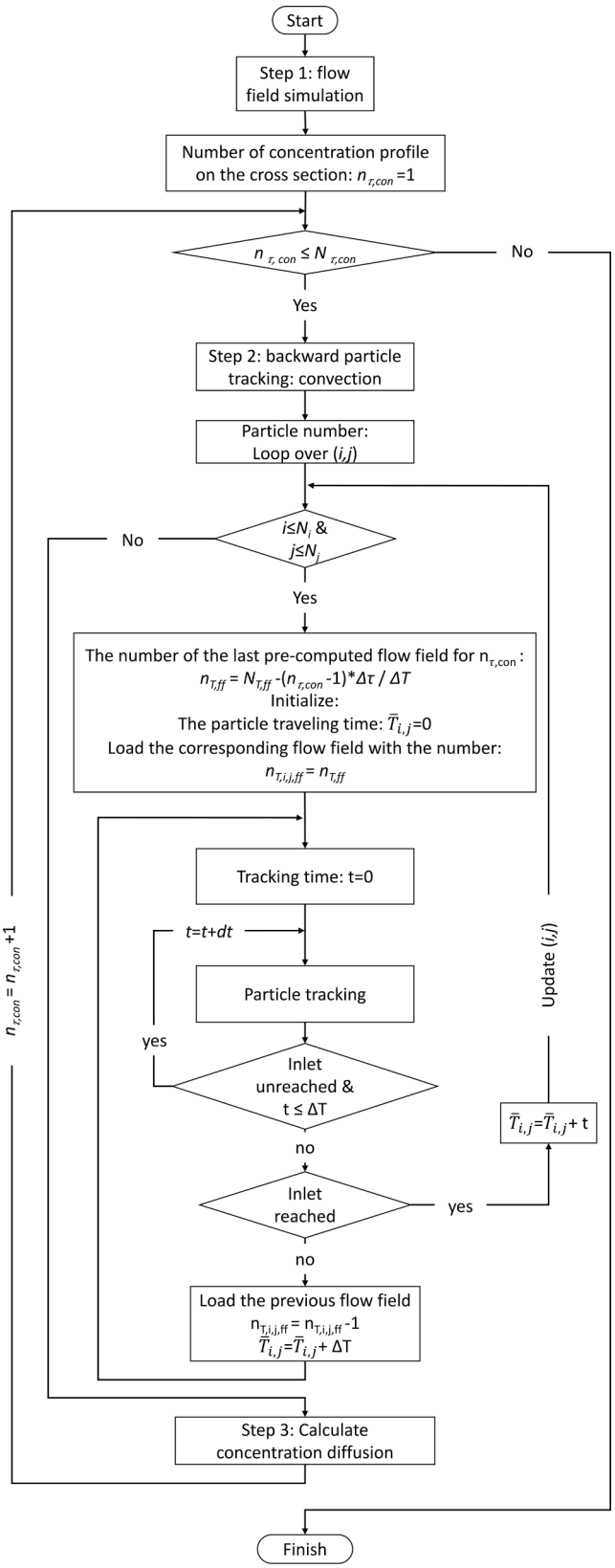

Fig. 2. Flow diagram of the algorithm. $N_{\tau,con}$ is the total number of concentration profiles in the video. $\Delta\tau$ is the time interval between two frames in the video. $N_{T,ff}$ represents the total number of the simulated flow field adopted for backward particle tracking. ΔT is the time interval between two saved flow fields. *i and j* denote the number of sampling particles in the z and x direction, respectively. N_i and N_j represent the total numbers of sampling particles for each frame in the z and x direction, respectively.

Fig. 1a, assuming that $T^k_{n+1} < T_n < T^{k+1}_{n+1}$. Then, the velocities and positions of sampling particles are recorded in a file and imported into Fluent for the backward particle tracking in period n with the next flow field. If a sampling particle is tracked until x = 20 mm in the fresh water inlet channel, the initial Rhodamine 6G concentration of a sampling particle, C^0_A, is 0. Similarly, if a sampling particle is tracked until x = −20 mm in the Rhodamine 6G inlet channel, C^0_A is 0.15 mg/L. Fig. 1c shows an exemplary convection contributed concentration profile with 300 × 150 sampling particles. The total traveling time of each sampling particle, $\overline{T}_{i,j}$, is also recorded.

$$\overrightarrow{F_d} = 3\pi\mu d_p(-\overrightarrow{u_w} - \overrightarrow{u_p}) \tag{4}$$

$$\overrightarrow{a} = \frac{d\overrightarrow{u_p}}{dt} = \frac{\overrightarrow{F_d}}{m} = \frac{3\pi\mu d_p(-\overrightarrow{u_w} - \overrightarrow{u_p})}{\frac{1}{6}\pi d_p^3\rho_p} \tag{5}$$

where, $\overrightarrow{u_p}$ is the velocity of the particle, m is the mass of the sampling particle, which is the product of the particle volume and density (Eq. (5)), d_p and ρ_p are the sampling particle diameter and density.

After one frame of convection-contributed concentration profile is obtained, another array of sampling points is set on the same cross-sectional plane and tracked back with the time interval Δτ of 0.1 s to simulate the next frame, which is done by starting with a different velocity field saved a time interval Δτ before the previous starting velocity field.

Lastly, the contribution of diffusion is estimated by integrating the Lagrangian scalar transport equation, as shown in Eq. (6). Theoretically, if both the initial concentration of a sampling particle and the diffusion rate along the pathline are known, the concentration can be solved. However, the diffusion rate is not known since the concentration field is not known. Thus, the overall diffusion rate is estimated by the diffusion rate on the interested cross-sectional plane [15]. The diffusion rate of a sampling particle with four neighbouring sampling particles is discretised as Eq. (7). The concentration of a sampling particle in the corner (shown in Fig. 1b) is set as the average concentration of two neighbouring particles as shown in Eq. (8). The concentration of a sampling point on the edge is set equal to its neighbour as shown in Eq. (9). Thus, a group of linear equations is established and solved by Matlab as shown in Eqs. (10) and (11).

$$C_A = C^0_A + D\int \nabla^2 C_A dt \approx C^0_A + D\overline{T}_{i,j}\left(\frac{\partial^2 C_A}{\partial x^2} + \frac{\partial^2 C_A}{\partial z^2}\right) \tag{6}$$

$$\frac{\partial^2 C_A}{\partial x^2} + \frac{\partial^2 C_A}{\partial z^2} = \frac{C_{i+1,j} + C_{i-1,j} + C_{i,j+1} + C_{i,j-1} - 4C_{i,j}}{dl^2} \tag{7}$$

$$C_{p,q} = \left(C_{p-1,q} + C_{p,q-1}\right)/2 \tag{8}$$

$$C_{m,n} = C_{m,n+1} \tag{9}$$

where, dl is the distance between two sampling particles as shown in Fig. 1b, $C_{p,q}$, $C_{p-1,q}$, $C_{p,q-1}$, $C_{m,n}$ and $C_{m,n+1}$ are shown in Fig. 1b.

$$C_{npar\times 1} = C^0_{npar\times 1} + A_{npar\times npar}C_{npar\times 1},$$

$$\text{with } C_{npar\times 1} = \begin{bmatrix} C_1 \\ C_2 \\ \vdots \\ C_{npar} \end{bmatrix}$$

$$C^0_{npar\times 1} = \begin{bmatrix} C^0_1 \\ C^0_2 \\ \vdots \\ C^0_{npar} \end{bmatrix} \tag{10}$$

$$C_{npar\times 1} = (I_{npar\times npar} - A_{npar\times npar})^{-1}C^0_{npar\times 1} \tag{11}$$

where, n_{par} denotes the number of sampling points, C_{npar*1} is the vector of concentrations of all sampling points, while $C^0_{npar\times 1}$ denotes the initial concentrations, $A_{npar\times npar}$ is the coefficient matrix determined by Eqs. (6)–(9), $I_{npar\times npar}$ is an identity matrix. The matrices are set as sparse matrices to accelerate the calculation.

Mixing index and mixing potential are adopted to quantify the mixing efficiency. Mixing index (MI) is estimated by Eq. (12) [6,25]. MI has a range from 0 to 1, where 0 indicates two totally segregated streams, while 1 suggests a perfectly mixed status. Mixing potential is used to quantify the specific contact area between two streams by Eq. (13), with a unit of m^2/m^3 [26].

$$MI = 1 - \sqrt{\frac{\sigma^2}{\sigma^2_{max}}}, \quad \text{with} \quad \sigma^2 = \frac{\int u_p{}^*(C_A - \overline{C_A})^2 dA}{\int u_p{}^* dA} \tag{12}$$

$$MP = \frac{\int \|\nabla f\| d\dot{V}}{\int d\dot{V}} = \frac{\int u_p{}^* \|\nabla f\| dA}{\int u_p dA} \quad \text{with} \quad f = \frac{C_A}{C_{A,max}} \tag{13}$$

where, σ^2 is the concentration variant, σ^2_{max} represents the maximum concentration variant before mixing, $\dot{V}$ is the volumetric flowrate, f is the normalized concentration, u_p denotes the velocity component perpendicular to the plane, A indicates the area of the cross-sectional plane.

3. Model validation and sensitivity analyses

The evolution of the concentration profile of the tracer inside the T mixer with two inlets is simulated by the proposed method based on the Lagrangian scalar transport equation. Reynolds number of two inlets is set as 237, implying the mixing process enters an unsteady regime [22].

In order to gain more understanding of the flow field, the velocities of three representative points, namely (0,0,0) mm, (0,5,0) mm and (0,20,0) mm, are monitored with time. Fig. S1a in the Supplementary Information shows that the calculated period of fluctuation is ~1.72 s, while the experimental results suggest that the period of fluctuation is about 1.9 s [22]. The difference in the period of fluctuation may come from the deviation from simulation and experimental conditions, since the rotameters have 2.5 % accuracy, or inaccuracy in simulating the flow field led by numerical dissipation.

To cover more than one period of the fluctuation, 20 frames ($N_{\tau,con}$ = 20) of concentration distributions are simulated for planes y = 5 mm, y = 25 mm and y = 45 mm, respectively. The time interval Δτ between two frames is 0.1 s, and the time interval between two flow fields during backward particle tracking, ΔT, is 0.05 s. The third order Monotonic Upstream-centred Scheme for Conservation Laws (MUSCL) method is also adopted coupling with the flow field to simulate the concentration profiles based on the Eulerian scalar transport equation, for comparison. The simulation results from the two methods are compared with the experimentally measured concentration distributions.

A time instant is selected in Fig. 3 to illustrate the accuracy of the method based on backward particle tracking. Fig. 3a-c show that the laminar structure captured by the camera is also reflected in the new approach. In contrast, the simulation results based on third order MUSCL highly overestimate the mixing efficiency due to numerical diffusion. Fig. 4c shows that the MI at y = 25 mm calculated by the new approach (300 × 150 sampling particles) is 0.044 ± 0.009, while the MI calculated by third order MUSCL is overestimated as 0.37 ± 0.06. Since the interface between the two streams is blurred by the third order MUSCL, the mixing potential simulated by the third order MUSCL is obviously lower than the MP from the new approach as shown in Fig. 4d. To further validate the simulation, the simulated concentrations along A-A′ at y = 5 mm and B-B′ at y = 25 mm are compared with experimental

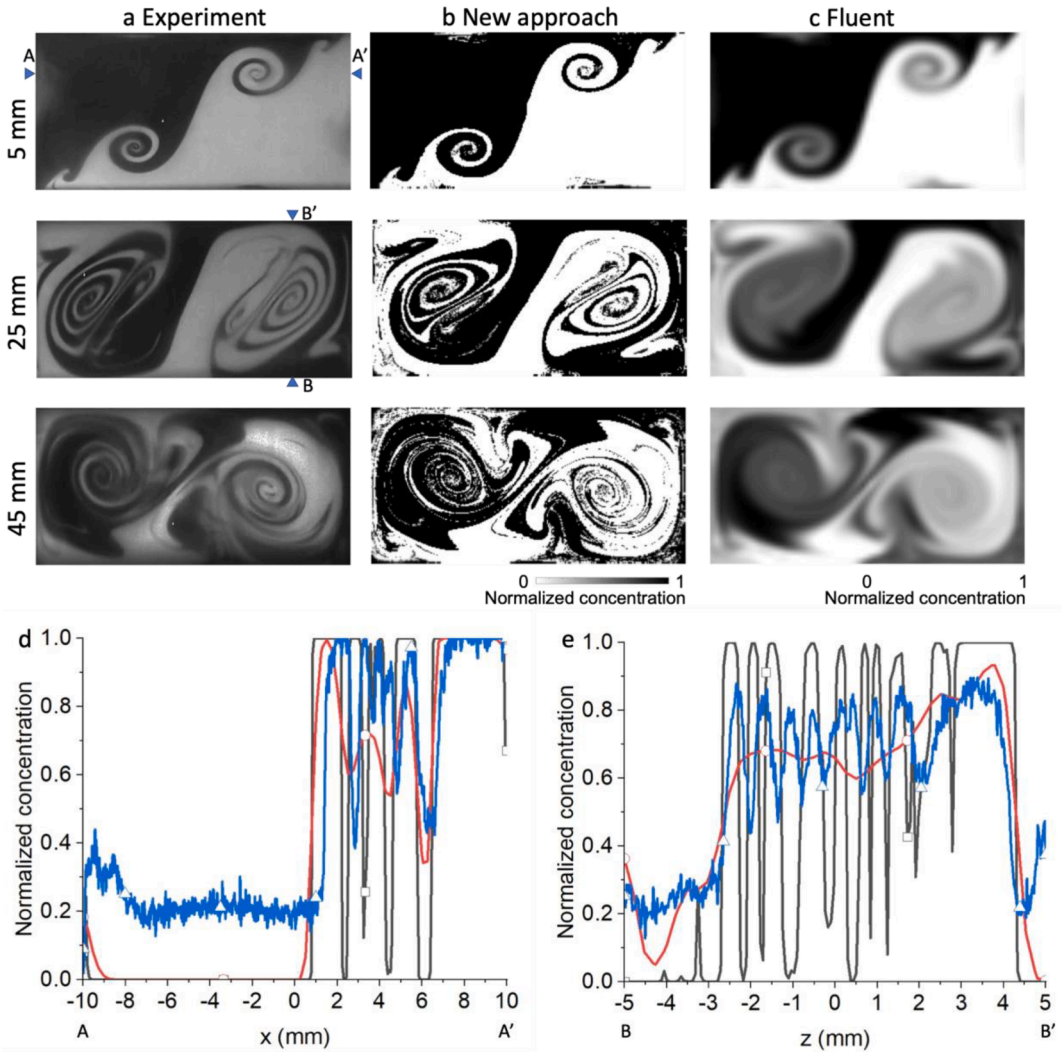

Fig. 3. Validation of the simulation method. a) Experimentally captured concentration profiles at a series of positions of the channel by planar laser-induced fluorescence, reprinted from [22], with permission from Elsevier. b) Simulation results by the novel approach based on backward particle tracking. c) Simulation results of the third order MUSCL scheme by Fluent. Comparison of experimentally captured concentration distribution of Rhodamine 6G (△) [22] and simulated concentration distributions by the new approach (□) and Fluent (○) d) along A-A′ at cross section y = 5 mm and e) along B-B′ at cross section y = 25 mm. Conditions: water temperature 15 °C, the diffusion coefficient of Rhodamine 6G 2.1 × 10^{-10} m^2/s, the Re at the inlets is 237, number of sampling points: 300 × 150, timestep 0.05 s, 3 million grids.

results, which has a layer thickness, δ, of 0.5 mm determined by the laser source [22]. Thus, taking A-A′ for example, the average concentration of the simulated concentrations at y = 5 − δ/2 mm, y = 5 mm and y = 5 + δ/2 mm is used for comparison. Fig. d and e show that the concentration distributions simulated by the new approach reasonably correlate well with the experimental results, identifying the laminar structures and enabling the estimation of mixing potential, while the third order MUSCL by Fluent highly overestimated diffusion and disabled the quantification of mixing potential. The discrepancy between experiment and simulation is partially attributed to the residual Rhodamine 6G on the wall which absorbs light in the experiment, with the lowest normalized concentration being ~0.2.

Note that the video of Fig. 3 is available in the online version, where 20 frames of experiments, the new approach and Fluent are compared. Again, the novel approach shows higher accuracy than the third order MUSCL by Fluent.

Fig. 4 a and b show that as the fluid travels from y = 5 mm to y = 25 mm and y = 45 mm, both the mixing index and mixing potential increase. There are two rotation centres in the channel because of the Kelvin-Helmholtz instability, which effectively blend two streams and increase the contact area between two streams. At y = 5 mm, MI within a period of fluctuation is 0.012 ± 0.002, and MP is 572 ± 111 m^2/m^3. At y = 45 mm, MI increases to 0.091 ± 0.011, and MP increases to 2309 ± 218 m^2/m^3.

It is important to note that the flow pattern and mixing efficiency in the *T*-mixer depend on Reynolds number. Thus, the flow fields and mixing efficiencies at 25 mm at a series of Reynolds number are simulated by the proposed method. As Re at the inlet channel increases from 10 to 100 and 150, the flow field is steady, and the flow pattern changes from strictly laminar flow at Re 10 to symmetric vortex flow at Re 100, and engulfment flow at Re 150, which is consistent with Dreher's study [16]. Further increase of Re to 200 and 237 leads to the unsteady periodic fluctuation. MIs at 25 mm are affected by both the mixing potential and average residence time. As shown in Fig. 5, MI decreases as Re increases from Re 10 to Re 100 due to the shorter average residence time, before MI increases to 0.039 ± 0.004 at Re 200 and 0.044 ± 0.009 at Re 237, respectively. Although the average residence time decreases as Re increases in the investigated range, the mixing potential increases from 68 m^2/m^3 to 138 m^2/m^3, 889 m^2/m^3, 1328 ± 189 m^2/m^3 and 1658 ± 241 m^2/m^3, respectively. It is expected that the high mixing

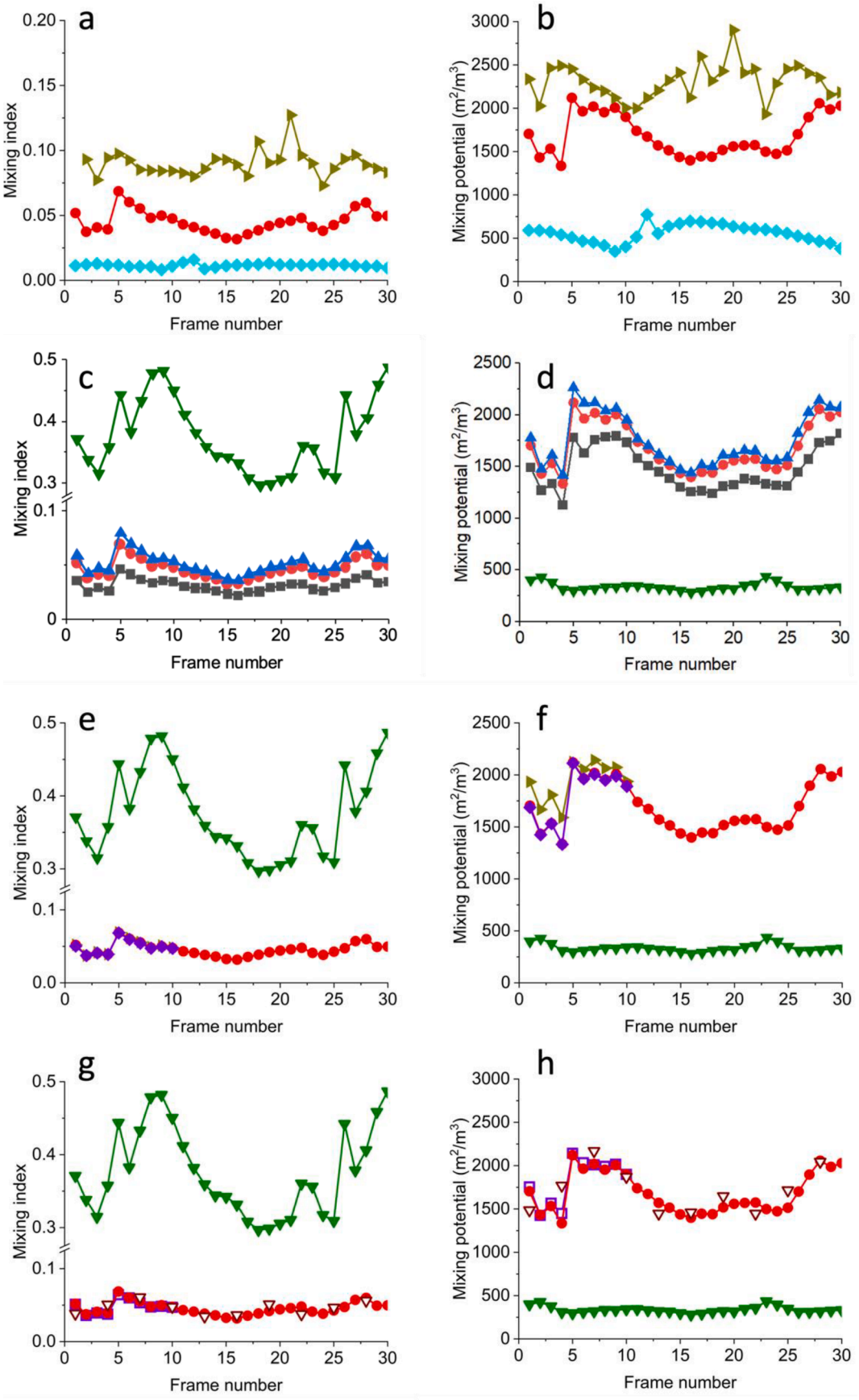

(caption on next page)

Fig. 4. Sensitivity analyses of the factors. a) Mixing indices and b) mixing potentials at y = 5 mm (◆), y = 25 mm (●) and y = 45 mm (▶), simulated with the following parameters: 300*150 sampling points, 0.04 s timestep ΔT. c) Mixing indices and d) mixing potentials of different frames calculated by different numbers of sampling points (200 × 100 ■, 300 × 150 ●, 360 × 180▲) on plane y = 25 mm, with a timestep ΔT of 0.04 s. The results of third order MUSCL by Fluent (▼) are presented for comparison purposes. e) Mixing indices and f) mixing potentials of different frames on plane y = 25 mm calculated by different sampling particle diameters (0.09 mm ◆, 0.1 mm ●, 0.11 mm ▶) for backward particle tracking, with 300*150 sampling points. The results from Fluent (▼) are presented for comparison purposes. g) Mixing indices and h) mixing potentials of different frames on plane y = 25 mm calculated by different time steps ΔT (0.02 s □, 0.04 s ●, 0.06 s ▽) for backward particle tracking, with 300*150 sampling points. The results from Fluent (▼) are presented for comparison purposes. Conditions: water temperature 15 °C, the diffusion coefficient of Rhodamine 6G 2.1 × 10^{-10} m^2/s, the Re at the inlets is 237, the time interval between two frames, Δτ, is 0.08 s, 3 million grids.

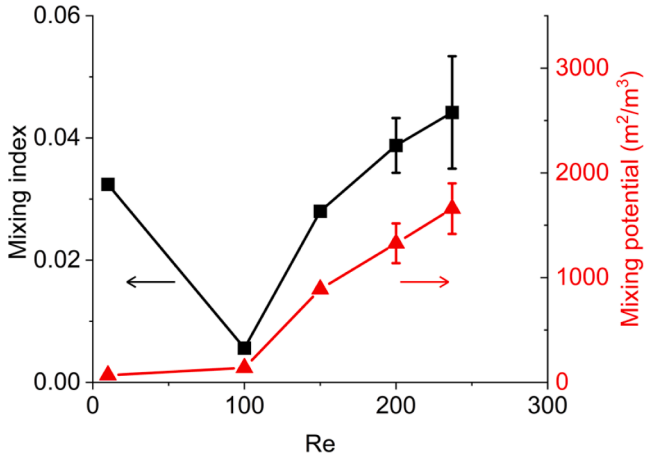

Fig. 5. Mixing indices (■) and mixing potentials (▲) at y = 25 mm as a function of Reynolds number at the inlet channel. The error bars represent the standard deviation of the values at unsteady state. Conditions: water temperature 15 °C, the diffusion coefficient of Rhodamine 6G 2.1 × 10^{-10} m^2/s, 3 million grids.

potential benefits diffusion in the downstream.

Sensitivity analyses are conducted to test the effects of four important factors on the simulated mixing index and mixing potential: the number of sampling particles, the diameter of sampling particles, the time interval ΔT between two flow fields during the backward particle tracking and the number of grids.

To test the effect of the number of sampling particles on simulated MI and MP, 200 × 100, 300 × 150, and 360 × 180 sampling particles are set on y = 25 mm, respectively. Other factors are kept constant: the time interval between two frames, Δτ, is 0.08 s, and the time interval between two flow fields during backward particle tracking, ΔT, is 0.04 s. Fig. 4c shows that the simulated mixing index and mixing potential by 200 × 100 sampling particles are smaller than 300 × 150 and 360 × 180. Indeed, the concentration profile by 200 × 100 sampling particles is actually coarser than the other two cases, as shown in Fig. S2. As the number of sampling particles increases to 300 × 150, MI and MP are similar to those simulated by 360 × 180 sampling particles, and the concentration profile by 300 × 150 is similar to that by 360 × 180 sampling particles. Considering the computational time, 300 × 150 sampling particles are selected for the other simulations.

To test the effect of the sampling particle diameter on simulation results, the diameter of sampling particles is set as 0.09 mm and 0.11 mm on y = 25 mm, respectively, except for the original 0.1 mm. Fig. 4e and f show that the simulated MI and MP with 0.1 mm and 0.11 mm sampling particle are similar with each other, while the 0.09 mm sampling diameter leads to a simulation uncertainty for MP. Thus, 0.1 mm sampling particle diameter is selected for the other simulations.

In order to test the effect of the time interval, Δτ, between two flow fields during backward particle tracking, 30 concentration profiles with time intervals Δτ 0.08 s and ΔT 0.04 s are simulated firstly. Then, 10 concentration profiles with ΔT of 0.02 s (Δτ 0.08 s) and 0.06 s (Δτ 0.12 s) are simulated, respectively. Thus, the frames at a series of moments can be compared directly, taking advantage of the same series of saved velocity fields with ΔT of 0.04 s.

Fig. 4g and h indicate that the simulated mixing indices and mixing potentials by different time intervals of backward particle tracking are similar, suggesting that 0.06 s time step is small enough to accurately simulate the results. Indeed, similar concentration profiles simulated with different time steps are presented in Fig. S3. Thus, 0.05 s time step for backward particle tracking is used to simulate the dynamic mixing process in Fig. 3.

To test the effect of the number of grids, 1.0 million, 3.0 million and 6.0 million cells are adopted respectively to simulate the flow field. Fig. S1b–d show that a small deviation is found between the velocities of three representative points calculated by 1.0 million and 3.0 million grids, while those by 3.0 million and 6.0 million are close. Thus, 3.0 million cells are adopted for all other simulations.

For the simulation of 30 concentration profiles at y = 25 mm with Δτ = 0.08 s and Δt = 0.04 s, a computer with 8 G memory and an I3 processor (3.6 GHz) takes about 60 h after the velocity field is solved. A considerable amount of time is spent on importing and exporting files by Fluent and Matlab, implying the potential to further reduce the time if the functions are integrated within one software.

In this study, the mixing efficiency inside an unsteady T mixer with a channel width of 20 mm at Re 237 is simulated. The method is valid for the simulation of diluted species mixing process if the incompressible Navier-Stokes equations apply. As the size of the mixer decreases to micrometers, both the mixing potential and pressure drop increase [23]. However, the high pressure drop may impede the endeavor to achieve the high mixing efficiency at unsteady state.

The method can be used to simulate the concentration profiles of diluted species at target cross sections, considering the physical mixing processes and ignoring chemical reactions. To simulate the whole concentration field, it is necessary to divide the volume to layers of volume pixels and run the simulation for each layer. Further work is required to simulate chemical reactions accurately.

4. Conclusions

The wide application of microreactors is partially attributed to the fast mixing performance. However, the mixing efficiency is difficult to quantify accurately, especially when the flow field is unsteady at high Re. In this paper, a novel method is developed to accurately simulate the unsteady mixing process in a *T*-mixer. The simulation method is based on the Lagrangian scalar transport equation solved by backward particle tracking. The simulation results are validated by experimentally measured tracer concentration profiles, and show much higher accuracy than the third order MUSCL based on the result of directly solving the Eulerian scalar transport equation. The method is expected to accelerate the development of highly efficient mixers, especially at unsteady laminar state, to satisfy material syntheses requesting fast mixing. It also paves the way for the establishment of simulation methods for the concentration field and reactions.

Declaration of Competing Interest

The authors declare that they have no known competing financial

interests or personal relationships that could have appeared to influence the work reported in this paper.

Data availability

Data will be made available on request.

Acknowledgements

The authors greatly acknowledge the insightful discussions and suggestions from Professor Laura Torrente Murciano. The authors sincerely thank Professor Weifeng Li and Mr Wei Zhang for kindly sharing the experimental data. This research did not receive any specific grant from funding agencies in the public, commercial, or not-for-profit sectors.

Appendix A. Supplementary data

Supplementary data to this article can be found online at https://doi.org/10.1016/j.cej.2023.141760.

References

[1] K.F. Jensen, Automated synthesis on a hub-and-spoke system, Nature 579 (2020) 346.
[2] K.F. Jensen, Microreaction Engineering— is small better? Chem. Eng. Sci. 56 (2) (2001) 293–303.
[3] Y. Gao, B. Pinho, L. Torrente-murciano, Recent progress on the manufacturing of nanoparticles in multi-phase and single-phase flow reactors, Curr. Opin. Chem. Eng. 29 (2020) 26–33, https://doi.org/10.1016/j.coche.2020.03.008.
[4] H. Kim, K.I. Min, K. Inoue, D.J. Im, D.P. Kim, J.I. Yoshida, Submillisecond organic synthesis: Outpacing Fries rearrangement through microfluidic rapid mixing, Science 352 (2016) 691–694, https://doi.org/10.1126/science.aaf1389.
[5] T. Schikarski, H. Trzenschiok, M. Avila, W. Peukert, Influence of Mixing on the Precipitation of Organic Nanoparticles: A Lagrangian Perspective on Scale-up Based on Self-Similar Distributions, Chem. Eng. Technol. 42 (2019) 1635–1642, https://doi.org/10.1002/ceat.201900095.
[6] Y. Gao, B. Pinho, L. Torrente-Murciano, Tailoring the size of silver nanoparticles by controlling mixing in microreactors, Chem. Eng. J. 432 (2021), 134112, https://doi.org/10.1016/j.cej.2021.134112.
[7] K.-J. Wu, G.M. De Varine Bohan, L. Torrente-Murciano, Synthesis of narrow sized silver nanoparticles in the absence of capping ligands in helical microreactors, React. Chem. Eng. 2 (2017) 116–128, https://doi.org/10.1039/C6RE00202A.
[8] M. Yang, L. Yang, J. Zheng, N. Hondow, R.A. Bourne, T. Bailey, G. Irons, E. Sutherland, D. Lavric, K. Wu, Mixing performance and continuous production of nanomaterials in an advanced-flow reactor, Chem. Eng. J. 412 (2021), 128565.
[9] M. Hoffmann, M. Schlüter, N. Räbiger, Experimental Analysis and Modeling of Micromixing in Microreactors, in: H. Bockhorn, D. Mewes, W. Peukert, H.-.-J. Warnecke (Eds.), Micro and Macro Mixing: Analysis, Simulation and Numerical Calculation, Springer Berlin Heidelberg, Berlin, Heidelberg, 2010, pp. 287–303, https://doi.org/10.1007/978-3-642-04549-3_16.
[10] S. Mitic, J.W. van Nieuwkasteele, A. van den Berg, S. de Vries, Design of turbulent tangential micro-mixers that mix liquids on the nanosecond time scale, Anal. Biochem. 469 (2015) 19–26, https://doi.org/10.1016/j.ab.2014.10.003.
[11] S. Hardt, T. Dietrich, A. Freitag, V. Hessel, H. Löwe, C. Hofmann, A. Groskar, F. Schönfeld, K. vanden Busche, Radial and tangential injection of liquid/liquid and gas/liquid streams and focusing thereof in a special cyclone mixer, in: IMRET, International Conference on Microreaction Technology, 6, AIChE Spring Meeting, 2002, 2002: pp. 329–342. https://www.tib.eu/de/suchen/id/tema%3ATEMA20030101724.
[12] K. Wang, H. Zhang, Y. Shen, A. Adamo, K.F. Jensen, Thermoformed fluoropolymer tubing for in-line mixing, React, Chem. Eng. 3 (2018) 707–713, https://doi.org/10.1039/c8re00112j.
[13] M. Guo, X. Hu, F. Yang, S. Jiao, Y. Wang, H. Zhao, G. Luo, H. Yu, Mixing Performance and Application of a Three-Dimensional Serpentine Microchannel Reactor with a Periodic Vortex-Inducing Structure, Ind. Eng. Chem. Res. 58 (2019) 13357–13365, https://doi.org/10.1021/acs.iecr.9b01573.
[14] R.T. Bailey, Managing false diffusion during second-order upwind simulations of liquid micromixing, Int. J. Numer. Methods Fluids. 83 (2017) 940–959, https://doi.org/10.1002/fld.4335.
[15] T. Matsunaga, H.J. Lee, K. Nishino, An approach for accurate simulation of liquid mixing in a T-shaped micromixer, Lab Chip. 13 (2013) 1515–1521, https://doi.org/10.1039/c3lc41009a.
[16] S. Dreher, N. Kockmann, P. Woias, Characterization of laminar transient flow regimes and mixing in t-shaped micromixers, Heat Transf. Eng. 30 (2009) 91–100, https://doi.org/10.1080/01457630802293480.
[17] S. Dreher, M. Engler, N. Kockmann, P. Woias, Theoretical and Experimental Investigations of Convective Micromixers and Microreactors for Chemical Reactions, in: H. Bockhorn, D. Mewes, W. Peukert, H.-J. Warnecke (Eds.), Micro and Macro Mixing: Analysis, Simulation and Numerical Calculation, Springer Berlin Heidelberg, Berlin, Heidelberg, 2010, pp. 325–346, https://doi.org/10.1007/978-3-642-04549-3_18.
[18] A. Mariotti, C. Galletti, M.V. Salvetti, E. Brunazzi, Unsteady Flow Regimes in a T-Shaped Micromixer: Mixing and Characteristic Frequencies, Ind. Eng. Chem. Res. 58 (2019) 13340–13356, https://doi.org/10.1021/acs.iecr.9b01259.
[19] J.M. MacInnes, A. Vikhansky, R.W.K. Allen, Numerical characterisation of folding flow microchannel mixers, Chem. Eng. Sci. 62 (2007) 2718–2727, https://doi.org/10.1016/j.ces.2007.02.014.
[20] M.Y. Kuo, C.Y. Wu, K.C. Hsu, C.Y. Chang, W. Jiang, Numerical investigation of high-peclet-number mixing in periodically curved microchannel with strong curvature, Heat Transfer Eng. 40 (2019) 1736–1749, https://doi.org/10.1080/01457632.2018.1497120.
[21] H. Talbi, E. Chaabelasri, M. Jeyar, N. Salhi, Random Walk Particle Tracking for Convection-diffusion Dominated Problems in Shallow Water Flows, J. Appl. Comput. Mech. 7 (2021) 486–495, https://doi.org/10.22055/jacm.2020.35154.2579.
[22] J. wei Zhang, S. fan Liu, C. Cheng, W. feng Li, X. lei Xu, H. feng Liu, F. chen Wang, Investigation of three-dimensional flow regime and mixing characteristic in T-jet reactor, Chem. Eng. J. 358 (2019) 1561–1573, https://doi.org/10.1016/j.cej.2018.10.112.
[23] Y. Gao, D.F. Zhu, Y. Han, L. Torrente-Murciano, Rational design of the inlet configuration of flow systems for enhanced mixing, J. Flow Chem. 11 (2021) 589–598.
[24] C. Galletti, M. Roudgar, E. Brunazzi, R. Mauri, Effect of inlet conditions on the engulfment pattern in a T-shaped micro-mixer, Chem. Eng. J. 185 (2012) 300–313, https://doi.org/10.1016/j.cej.2012.01.046.
[25] T. Matsunaga, K. Nishino, Swirl-inducing inlet for passive micromixers, RSC Adv. 4 (2014) 824–829, https://doi.org/10.1039/c3ra44438d.
[26] D. Bothe, C. Stemich, H.J. Warnecke, Fluid mixing in a T-shaped micro-mixer, Chem. Eng. Sci. 61 (2006) 2950–2958, https://doi.org/10.1016/j.ces.2005.10.060.